

# Boreal Winter Surface Air Temperature Responses to Large Tropical Volcanic Eruptions in CMIP5 Models

CHEN XING AND FEI LIU

*Earth System Modeling and Climate Dynamics Research Center, Nanjing University of Information Science and Technology, Nanjing, China*

BIN WANG

*Department of Atmospheric Sciences and Atmosphere–Ocean Research Center, University of Hawai‘i at Mānoa, Honolulu, Hawaii*

DELIANG CHEN

*Department of Earth Sciences, University of Gothenburg, Gothenburg, Sweden*

JIAN LIU AND BIN LIU

*Key Laboratory of Virtual Geographic Environment of Ministry of Education, School of Geography Science, Nanjing Normal University, Nanjing, China*

(Manuscript received 6 March 2019, in final form 16 December 2019)

## ABSTRACT

We analyzed global surface air temperature (SAT) responses to five major tropical volcanic eruptions from 1870 to 2005 using outputs from 97 historical and 58 Atmospheric Model Intercomparison Project (AMIP) runs that participated in phase 5 of the Coupled Model Intercomparison Project (CMIP5). In observations, there was a 3-yr global cooling trend after the eruption due to reduced shortwave radiation, and a 0.1-K average global-mean SAT recovery, consisting of El Niño-like tropical warming and Eurasian warming, occurred in the first posteruption boreal winter. This global cooling pause was simulated by the multimodel ensemble (MME) mean of the AMIP runs, but not the MME of the historical runs due to the absence of El Niño-like warming. In the historical runs, simulation of El Niño-like warming was influenced by the initial ocean condition (IOC). An El Niño-like response was simulated when the IOC was not in an El Niño state, but the warming was much weaker compared to observations. The Eurasian warming response, despite being reproduced by the MME mean of both AMIP and historical runs, was not as strong as in observations. This is because the simulated positive polar vortex response, an important stratospheric forcing for Eurasian warming, was very weak, which suggests that the CMIP5 models, and even the Climate Forecast System model, underestimate volcanic effects on the stratosphere. Most of the coupled models failed to replicate both the El Niño and the enhanced polar vortex responses, indicating an urgent need for improving air–sea interaction and stratospheric processes in these models.

## 1. Introduction

Large volcanic eruptions provide an important external forcing that has caused significant global surface cooling typically lasting for 3 years (Crowley 2000; Hegerl et al.

2003; Mann et al. 1998; Robock 2000; Sear et al. 1987; Timmreck 2012). This cooling process starts when a large amount of SO<sub>2</sub> gas injected into the stratosphere reacts with OH and H<sub>2</sub>O to form sulfate aerosols, which can perturb the radiative balance (Robock 2000). For example, the year after the strong eruption of Tambora in 1815 is known as the year without a summer (Oppenheimer 2003). Surface cooling, however, is not always the case after a large tropical eruption. The volcanic eruption-induced global cooling was absent due to El Niño in the

 Denotes content that is immediately available upon publication as open access.

Corresponding author: Dr. Fei Liu, liuf@nuist.edu.cn

DOI: 10.1175/JCLI-D-19-0186.1

© 2020 American Meteorological Society. For information regarding reuse of this content and general copyright information, consult the [AMS Copyright Policy](#) ([www.ametsoc.org/PUBSReuseLicenses](http://www.ametsoc.org/PUBSReuseLicenses)).

first posteruption boreal winter after the 1963 Agung eruption (Lehner et al. 2016) and the 1982 El Chichón eruption (Lehner et al. 2016; Santer et al. 2014), thereby forming a pause in the 3-yr global cooling following those tropical eruptions.

Changes in global mean surface air temperature (SAT) are controlled not only by external forcing but also by El Niño–Southern Oscillation (ENSO). Over the past decades, a positive global mean SAT anomaly is usually related to El Niño (Trenberth 2002; Trenberth and Fasullo 2013), which is the warm phase of ENSO. Global cooling emerges after a large volcanic eruption when the El Niño signal is removed from observations (Angell 1988; Gu and Adler 2011; Nicholls 1988; Thompson et al. 2009), from simulations (Paik and Min 2016), or from both observations and model simulations (Santer et al. 2014; Soden et al. 2002), which suggests that ENSO may be one reason for the inconsistency in global cooling in the first boreal winter after a large volcanic eruption.

El Niño occurred after four of the five large volcanic eruptions during 1870–2005 (Khodri et al. 2017). The relationship between El Niño events and volcanic eruptions in this period was originally considered a coincidence (Robock 2000; Self et al. 1997). However, analyses of long-term reconstruction data have suggested that large tropical eruptions can increase the likelihood of El Niño (Adams et al. 2003; Liu et al. 2018b), mainly through the dynamic thermostat mechanism (Clement et al. 1996; Maher et al. 2015; Mann et al. 2005; Ohba et al. 2013; Predybaylo et al. 2017) and also via other mechanisms as reviewed in Liu et al. (2018a).

Surface warming over the Eurasian continent was also observed to reach a maximum of 3 K in the first boreal winter after the 1991 Pinatubo eruption (Robock 2002; Robock and Mao 1992), which might also contribute to the global cooling pause following the eruption. The stratospheric pathway is a potential explanation for this boreal-winter warming after a large eruption. Volcanic aerosols from a large tropical eruption warm the low-latitude lower stratosphere; the resulting temperature gradient toward the equator decreases the high-latitude geopotential height and strengthens the stratospheric polar vortex (Robock 2000; Stenchikov et al. 2002). Positive westerly anomalies associated with enhanced polar vortex will trap tropospheric wave energy via planetary wave reflection (Graf et al. 2007; Perlwitz and Harnik 2003). In addition, the positive Arctic Oscillation or the North Atlantic Oscillation (NAO) dominates the boreal winter circulation, resulting in Eurasian winter warming from January to February (Graf et al. 2014; Perlwitz and Graf 1995).

It is not clear whether the state-of-the-art models in phase 5 of the Coupled Model Intercomparison Project

(CMIP5) can simulate the pause of global cooling, including both tropical El Niño–like warming and Eurasian warming, during the first boreal winter of the 3-yr global cooling after a large tropical eruption. Although the models successfully reproduce El Niño responses in the Pacific sea surface height, their multimodel ensemble (MME) mean usually fails to simulate the observed response in sea surface temperature (SST) to the large tropical volcanic eruptions during the period of 1870–2005 (Ding et al. 2014; Maher et al. 2015). Focusing on the largest eruptions of Krakatau and Pinatubo, Zambri and Robock (2016) reported that some CMIP5 models replicate the observed warming over northern Europe and Asia and the observed polar vortex enhancement in the first posteruption boreal winter. When some relatively weaker eruptions are included, the CMIP5 models generally fail to capture the dynamic responses in the Northern Hemisphere (NH) after most tropical eruptions, such as the NAO, polar vortex, and Eurasian warming (Bittner et al. 2016; Driscoll et al. 2012).

In this work, we investigate the fidelity of SAT responses in CMIP5 models during the first boreal winter after a large tropical volcanic eruption. The paper is organized as follows. In section 2, we present the data and methods. Simulations of global cooling pause and El Niño response are discussed in section 3. The Eurasian SAT and polar vortex responses are the foci of section 4. In section 5, we discuss the internal variability–induced global cooling pause in the Community Earth System Model Large Ensemble (CESM-LE). Conclusions are given in section 6.

## 2. Data and methods

Monthly reanalysis data of geopotential height, air temperature, and zonal wind were obtained from 1) the Twentieth Century Reanalysis version 2c (20CRv2c; Compo et al. 2011) for the period of 1851–2014 and 2) the Japanese 55-year Reanalysis (JRA-55; Kobayashi et al. 2015) for the period of 1958–2013. The long-term observed monthly SAT field from 1870 to 2018 was also used; the data were from the 1200-km smoothed NASA Goddard Institute for Space Studies (GISS) Surface Temperature Analysis (GISTEMP) version 3 (Lensen et al. 2019). Monthly SST data were from the following sources: 1) the Extended Reconstructed Sea Surface Temperature dataset version 5 (ERSSTv5; Huang et al. 2017) for the period of 1854–2017, 2) the Hadley Centre Sea Ice and Sea Surface Temperature dataset version 1 (HadISST1; Rayner et al. 2003) for the period of 1870–2016, and 3) the uninterpolated Second Hadley Centre Sea Surface Temperature dataset (HadSST2; Rayner et al. 2006) for the period of 1850–2004.

TABLE 1. List of five major tropical volcanic eruptions since 1870 used in this study. The volcanic strength is shown by the maximum monthly value of global mean aerosol optical depth (AOD) at 550 nm (Sato et al. 1993), the ice-core volcanic index 2 (IVI2) stratospheric sulfate injections (Gao et al. 2008), and the volcanic explosivity index (VEI; Newhall and Self 1982). The VEI values are obtained from <http://www.volcano.si.edu>.

Name	Date	Location	AOD (550 nm)	IVI2 (Tg)	VEI
Krakatau	26–27 Aug 1883	6.1°S, 105.4°E	0.16	22	6
Santa Maria	24–25 Oct 1902	14.8°N, 91.6°W	0.08	4	5
Agung	17 Mar, 16 May 1963	8.3°S, 115.5°E	0.09	17	5
El Chichón	3–4 Apr 1982	17.4°N, 93.2°W	0.10	14	5
Pinatubo	15 Jun 1991	15.1°N, 120.4°W	0.15	30	6

Five large tropical volcanic eruptions during 1870–2005 were selected in this study, namely, the eruption of Krakatau in August 1883, of Santa Maria in October 1902, of Agung in March 1963, of El Chichón in April 1982, and of Pinatubo in June 1991 (Table 1). They have the five largest aerosol optical depths (AOD) at 550 nm among the tropical volcanic eruptions since 1870 (Khodri et al. 2017; Sato et al. 1993). The eruption season, which has been found to affect atmospheric circulation responses in simulations (McGregor and Timmermann 2011; Predybaylo et al. 2017; Stevenson et al. 2017), was not considered in this work. Since the global cooling pause as well as the El Niño and Eurasian SAT responses peaked in the first posteruption boreal winter, we use calendar months rather than the months after the eruption peak in our study.

Table 2 gives details of the 32 coupled general climate models (GCMs) for historical runs covering the period of 1870–2005 (Taylor et al. 2012). The 17 atmospheric GCMs for the Atmospheric Model Intercomparison Project (AMIP) runs covering the period of 1979–2005, along with observed SSTs and sea ice (Taylor et al. 2012) used in the AMIP runs, are also introduced in the table. The models in the historical and AMIP runs were forced by both anthropogenic and natural forcing, including the five large tropical eruptions in the historical runs and the latest 1982 El Chichón and 1991 Pinatubo eruptions in the AMIP runs. Due to the important role of large ensemble members in detecting responses of ENSO (Maher et al. 2018) and NH polar vortex (Bittner et al. 2016) to volcanic forcing, 97 available ensemble members of the historical runs for the 32 models and 58 available ensemble members of the AMIP runs for the 17 AMIP models were considered. Table 2 also lists the volcanic forcing datasets used for these five eruptions, which were obtained from Sato et al. (1993), Andres and Kasgnoc (1998), Stenchikov et al. (1998), Ammann et al. (2003), and Ammann et al. (2007). Models adopting insolation reduction rather than aerosol forcing were not considered in this work. All model outputs were interpolated onto  $2.5^\circ \times 2.5^\circ$  grid using bilinear interpolation. For surface temperature, 2-m SAT was used.

In addition, we employed the fully coupled CESM-LE, which has 41 ensemble members at roughly  $1^\circ$  resolution for 1920–2005 following the historical run's setup and contains three selected eruptions, namely the 1963 Agung, 1982 El Chichón, and 1991 Pinatubo eruptions. A full description of the CESM-LE can be found in Kay et al. (2015).

To isolate climate responses to the five eruptions from the background noise, we obtained anomalies by removing the average of climatology in the five years preceding each eruption. The long-term linear trend was also removed. Since the AMIP runs started from 1979, we used the average of climatology in the three years preceding the 1982 El Chichón eruption. When calculating the MME mean, averages were taken among ensemble members of each model first before getting the multimodel mean; in this way, all models were given equal weight. Similar results were also obtained by directly performing the average across ensemble members of all models without considering model bias (not shown).

Significance was calculated using the bootstrapped resampling method with 10 000 times of random synthesis across the whole period, and the 95% confidence level came from the 2.5%–97.5% range of the 10 000 draws. For the MME mean, we calculated the number of models that agreed on the sign of the response. In this way, the overall response could be considered without disturbances from large responses that may be dominated by only a few models (Barnes et al. 2016; Zambri and Robock 2016). If the data were purely random, for the historical runs the probability of at least 22 of the 32 models agreeing on the sign of the response was 5.0% with calculation based on the binomial distribution, which equaled the typical 95% confidence limit. For the AMIP runs, the probability of at least 13 of the 17 models agreeing on the sign of the response was 4.9%, which was close to the typical 95% confidence limit.

The Niño-3.4 index was defined as the SST anomaly averaged over the region of  $5^\circ\text{S}$ – $5^\circ\text{N}$ ,  $170^\circ$ – $120^\circ\text{W}$ . We also used the relative SST anomaly reflecting the tendency of ENSO isolated from volcanically induced surface cooling (Khodri et al. 2017), which was obtained by

TABLE 2. Information on CMIP5 models used: modeling center, model name, number of ensemble members, resolution, and volcanic forcing; "A" and "H" represent the AMIP and historical runs, respectively. (Expansions of acronyms are available online at <http://www.ametsoc.org/Pubs/AcronymList>.)

Modeling center	Model name	No. of ensemble members (A/H)	Resolution (latitude grid $\times$ longitude grid $\times$ vertical level)	Volcanic forcing dataset	Reference
Commonwealth Scientific and Industrial Research Organization/Bureau of Meteorology (CSIRO-BOM)	ACCESS1.0	1/1	145 $\times$ 192 $\times$ 38	Sato et al. (1993)	Bi et al. (2013)
	ACCESS1.3	1/1	145 $\times$ 192 $\times$ 38	Sato et al. (1993)	Bi et al. (2013)
Beijing Climate Center (BCC)	BCC-CSM1.1	3/3	64 $\times$ 128 $\times$ 26	(Ammann et al. 2003)	(Wu et al. 2013)
	BCC-CSM1.1-m	3/3	160 $\times$ 320 $\times$ 26	(Ammann et al. 2003)	(Wu et al. 2013)
Canadian Centre for Climate Modeling and Analysis (CCCma)	CanESM2	0/5	64 $\times$ 128 $\times$ 35	(Sato et al. 1993)	(Chylek et al. 2011)
	CanAM4	4/0	64 $\times$ 128 $\times$ 35	(Sato et al. 1993)	(Chylek et al. 2011)
National Center for Atmospheric Research (NCAR)	CCSM4	6/6	192 $\times$ 288 $\times$ 26	(Ammann et al. 2003)	(Gent et al. 2011)
	CESM1-BGC	0/1	192 $\times$ 288 $\times$ 30	(Ammann et al. 2003)	(Hurrell et al. 2013)
	CESM1-CAM5	2/3	192 $\times$ 288 $\times$ 30	(Ammann et al. 2003)	(Neale et al. 2010)
	CESM1-CAM5.1-FV2	0/1	96 $\times$ 144 $\times$ 30	(Ammann et al. 2003)	(Neale et al. 2010)
Centre National de Recherches Météorologiques, Centre Européen de Recherche et de Formation Avancée en Calcul Scientifique (CNRM-CERFACS)	GESM1-FASTCHEM	0/3	192 $\times$ 288 $\times$ 30	(Ammann et al. 2003)	(Hurrell et al. 2013)
	GESM1-WACCM <sup>a</sup>	0/1	96 $\times$ 144 $\times$ 66	(Ammann et al. 2003)	(Hurrell et al. 2013)
Commonwealth Scientific and Industrial Research Organization/Queensland Climate Change Centre of Excellence (CSIRO-QCCCCE)	GNRM-CM5	1/10	128 $\times$ 256 $\times$ 31	(Ammann et al. 2007)	(Voldoire et al. 2013)
	CNRM-CM5.2	0/1	128 $\times$ 256 $\times$ 60	(Ammann et al. 2007)	(Voldoire et al. 2013)
Commonwealth Scientific and Industrial Research Organization/Queensland Climate Change Centre of Excellence (CSIRO-QCCCCE)	CSIRO-Mk3.6.0	0/10	96 $\times$ 192 $\times$ 18	(Sato et al. 1993)	(Rotstayn et al. 2009)
Geophysical Fluid Dynamics Laboratory (NOAA/GFDL)	GFDL-CM3	5/5	90 $\times$ 144 $\times$ 48	(Sato et al. 1993; Stenchikov et al. 1998)	(Donner et al. 2011)
	GFDL-ESM2G	0/1	90 $\times$ 144 $\times$ 24	(Sato et al. 1993)	(Dunne et al. 2012)
Geophysical Fluid Dynamics Laboratory (NOAA/GFDL)	GFDL-ESM2M	0/1	90 $\times$ 144 $\times$ 24	(Sato et al. 1993)	(Dunne et al. 2012)
	GFDL-HIRAM-C180	3/0	360 $\times$ 571 $\times$ 32	(Sato et al. 1993)	(Zhao et al. 2009)
	GFDL-HIRAM-C360	2/0	900 $\times$ 1200 $\times$ 32	(Sato et al. 1993)	(Zhao et al. 2009)

TABLE 2. (Continued)

Modeling center	Model name	No. of ensemble members (A/H)	Resolution (latitude grid $\times$ longitude grid $\times$ vertical level)	Volcanic forcing dataset	Reference
Goddard Institute for Space Studies (NASA GISS)	GISS-E2-H	0/6	90 $\times$ 144 $\times$ 40	(Sato et al. 1993)	(Schmidt et al. 2014)
	GISS-E2-H-CC	0/1	90 $\times$ 144 $\times$ 40	(Sato et al. 1993)	(Schmidt et al. 2014)
	GISS-E2-R	6/6	90 $\times$ 144 $\times$ 40	(Sato et al. 1993)	(Schmidt et al. 2014)
	GISS-E2-R-CC	0/1	90 $\times$ 144 $\times$ 40	(Sato et al. 1993)	(Schmidt et al. 2014)
	HadGEM2-AO	0/1	145 $\times$ 192 $\times$ 38	(Sato et al. 1993)	(Martin et al. 2011)
National Institute of Meteorological Research, Korea Meteorological Administration (NIMR)	HadGEM2-A	1/0	145 $\times$ 192 $\times$ 38	(Sato et al. 1993)	(Martin et al. 2011)
	HadGEM2-ES	0/4	145 $\times$ 192 $\times$ 38	(Sato et al. 1993)	(Martin et al. 2011)
	MIROC5	2/5	128 $\times$ 256 $\times$ 40	(Sato et al. 1993)	(Watanabe et al. 2010)
Atmosphere and Ocean Research Institute (The University of Tokyo), National Institute for Environmental Studies, and Japan Agency for Marine-Earth Science and Technology (MIROC)	MIROC-ESM-CHEM	0/1	64 $\times$ 128 $\times$ 80	(Sato et al. 1993)	(Watanabe et al. 2011)
	MPI-ESM-LR	3/3	96 $\times$ 192 $\times$ 47	(Stenchikov et al. 1998)	(Giorgetta et al. 2013)
Max Planck Institute for Meteorology (MPI-M)	MPI-ESM-MR	3/3	96 $\times$ 192 $\times$ 95	(Stenchikov et al. 1998)	(Giorgetta et al. 2013)
	MPI-ESM-P	0/2	96 $\times$ 192 $\times$ 47	(Stenchikov et al. 1998)	(Giorgetta et al. 2013)
	MRI-CGCM3	0/3	160 $\times$ 320 $\times$ 48	(Andres and Kasgnoc 1998)	(Yukimoto et al. 2012)
Meteorological Research Institute (MRI)	MRI-ESM1	0/1	160 $\times$ 320 $\times$ 48	(Andres and Kasgnoc 1998)	(Yukimoto 2011)
	NorESM1-M	3/3	96 $\times$ 144 $\times$ 26	(Ammann et al. 2003)	(Bentsen et al. 2013)
	NorESM1-ME	0/1	96 $\times$ 144 $\times$ 26	(Ammann et al. 2003)	(Bentsen et al. 2013)

<sup>a</sup> Although there are four ensemble members for CESM1-WACCM, the last three start from 1955, so we only use the first ensemble.

removing the average of the tropical ( $20^{\circ}\text{S}$ – $20^{\circ}\text{N}$ ) SST anomaly from the original SST anomaly. To describe the stratospheric response in the North Pole region, the polar vortex index was defined as the inverted geopotential height anomaly averaged over the North Pole ( $65^{\circ}$ – $90^{\circ}\text{N}$ ,  $0^{\circ}$ – $360^{\circ}$ ) at 50 hPa during the boreal winter. Here, boreal winter refers to December–February (DJF). Year (0) is defined as the eruption year, and year (–1) represents the year before the eruption.

### 3. Global cooling pause and El Niño response

Figure 1 shows the global mean SAT anomalies for the five large tropical volcanic eruptions and their composite values from observations and simulations. After each of the five eruptions, there was a cooling trend in the following three years (Fig. 1a). However, a global cooling pause against the monotonous cooling trend in global mean SAT also existed in GISTEMP during the first boreal winter after each eruption (hereafter the first boreal winter). Similar results can also be found in the Hadley Centre Climatic Research Unit surface temperature version 4 (HadCRUT4; Morice et al. 2012) and 20CRv2c. In this first boreal winter, the averaged global mean SAT recovery, which was identified by the difference between the original and 3-yr low-pass SAT, can reach 0.1 K for the average of the five eruptions. Figure 1b shows the MME mean of simulated global mean SAT anomalies for these tropical eruptions in the historical and AMIP runs of CMIP5 models. A significant cooling trend in the three years following each of these large eruptions was simulated in both the historical and AMIP runs (Fig. 1b), which is consistent with observations. Maximum cooling in the MME mean of the 32 historical models reaches 0.3 K in the boreal summer of the second posteruption year. The first-boreal-winter global cooling pause is reproduced by the MME mean of the AMIP runs, but is not adequately simulated by the MME mean of the historical models, which only exhibits a monotonous cooling trend. In summary, the MME mean of the CMIP5 models replicates global cooling in the three years following the large tropical eruptions but does not adequately simulate the first-boreal-winter response.

Figure 2 shows composite global SAT anomalies during the first boreal winter after the eruption in reanalysis, observations, and simulations. In 20CRv2c (Fig. 2a), a pause in global cooling during the first boreal winter appears as significant El Niño warming in the tropics and strong warming in Eurasia, which is consistent with previous finding (Robock and Mao 1992). Eurasian warming occurs during the first post-eruption boreal winter after four of the five large tropical eruptions, with the 1963 Agung eruption being the

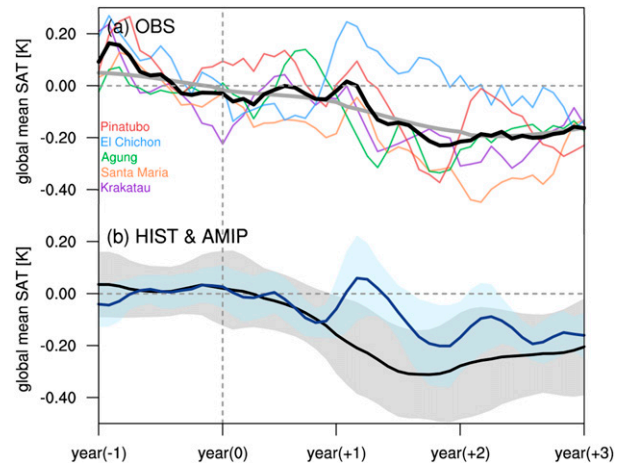


FIG. 1. Observed and simulated responses of global mean surface air temperature (SAT) to five major tropical eruptions. (a) Evolution of observed 3-month-moving-averaged global mean SAT anomaly with respect to the five years preceding the eruption (thin curves) in the observations of GISTEMP during 1870–2014, and the average of the five eruptions (black thick curve). The thick gray line indicates 3-yr low-pass global mean SAT anomaly of GISTEMP. (b) As in (a), but for the historical runs (black) and AMIP runs (blue; only for the last two eruptions). The shading indicates one standard deviation among the models; “0” denotes the eruption year, and “–1/+1” indicates one year before/after the eruption. The dashed vertical line indicates January of the eruption year.

only exception. Similar patterns can also be found in the observations of GISTEMP (Fig. 2b) and HadCRUT4 (not shown).

In the MME mean of the AMIP runs (Fig. 2c), the significant SAT response over the ocean is similar to that of the observations due to specified SST; a positive Pacific–North American (PNA)-like pattern in SAT is also seen from the tropical Pacific to North America, with positive–negative–positive–negative anomalies over the central Pacific, North Pacific, Canada, and southeastern United States. The Eurasian warming response in the first boreal winter, however, is much weaker in the models than in observations. Without the specified SST, the MME mean of the historical runs exhibited significant global cooling over low-latitude regions, with weak warming only occurring over the NH polar region (Fig. 2d). The El Niño-like response is not simulated by the MME mean of the historical runs.

In summary, global cooling in the three years following each of the five large tropical eruptions is simulated by both the historical and AMIP runs. The MME mean of the AMIP runs reproduces the first-boreal-winter SAT responses well, while that of the historical runs does not. One major difference between the historical and AMIP runs is the El Niño signal in the tropical Pacific, which is closely connected to global temperature

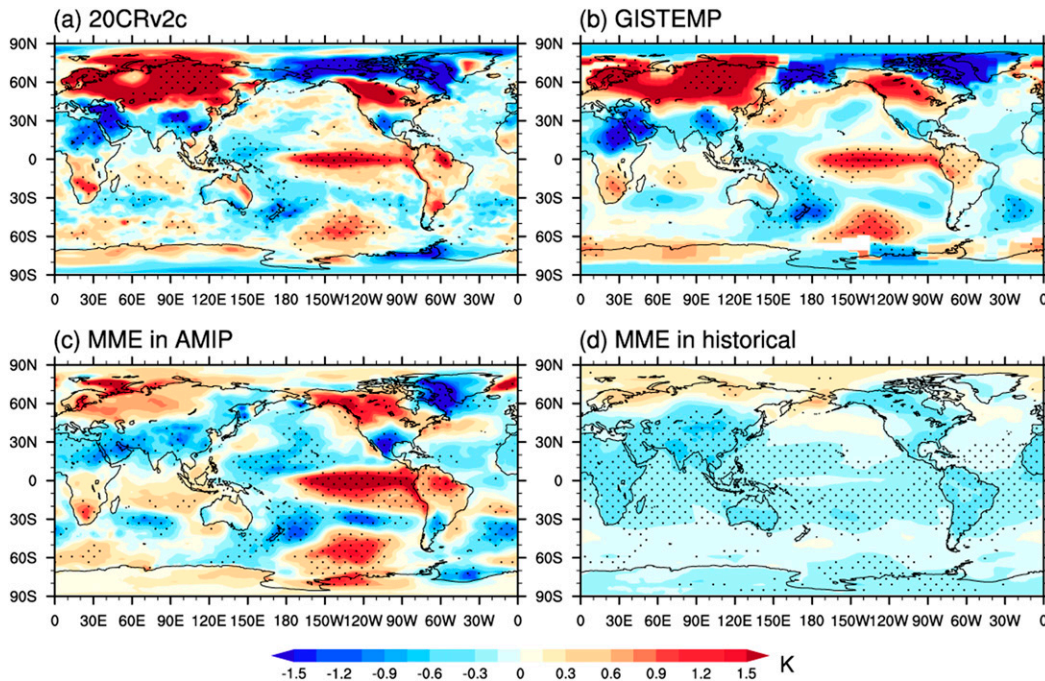


FIG. 2. Observed and simulated boreal-winter SAT anomaly after the eruptions. Composite SAT anomaly (shading; K) with respect to the five years preceding each eruption during the first boreal winter after the five selected eruptions in (a) 20CRv2c, (b) GISTEMP, (c) MME mean of AMIP runs (the last two eruptions only), and (d) MME mean of historical runs. Stippling indicates temperature anomaly significant at the 95% confidence level, which means that more than 13 of the 17 AMIP models and more than 22 of the 32 CMIP5 models of historical run agree on the sign of the anomaly.

anomalies through teleconnection caused by latent heating (Trenberth 2002). The Niño-3.4 index for these five tropical eruptions is shown in Fig. 3 for both observations and historical runs. In the three observational datasets, most of the eruptions were followed by El Niño events in the first boreal winter (Fig. 3a). The 1883 Krakatau eruption, being the only exception, was followed by a neutral ENSO response. Four of the five eruptions showed both global cooling pause and positive Niño-3.4 anomalies in the first boreal winter, while the 1883 Krakatau eruption only yielded a global cooling pause and a neutral ENSO response. The global cooling pause and El Niño response after the 1982 El Chichón eruption were stronger than those of the others (Figs. 1a and 3a). In the AMIP runs from 1979 to 2005, observational El Niño SST was specified as part of the forcing for the 1982 and 1991 boreal winters, while the MME mean of the historical runs from year (0) to year (2) only simulates a neutral ENSO response (Fig. 3b).

Since there is a close relationship between global mean SAT and ENSO (Trenberth 2002; Trenberth and Fasullo 2013), the observed and simulated ENSO and global mean SAT responses in the first boreal winter after each of these eruptions are exhibited in Fig. 4. Global mean SAT anomalies in the first boreal winter,

accompanied by warm ENSO events, are nearly neutral or positive against the cooling trend in both observational mean and MME mean of the AMIP runs. Besides, the simulated global mean SAT anomalies in the MME mean of the AMIP runs are cooler than the observational mean for the 1982 El Chichón and 1991 Pinatubo

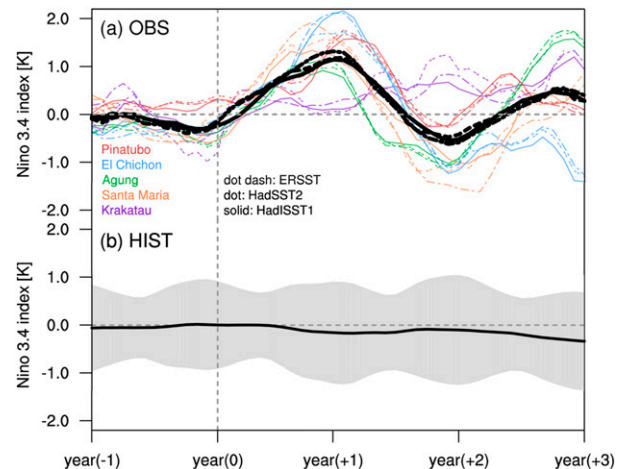


FIG. 3. As in Fig. 1, but for the Niño-3.4 index using (a) three observational datasets of HadISST1, HadSST2, and ERSST and (b) historical runs.

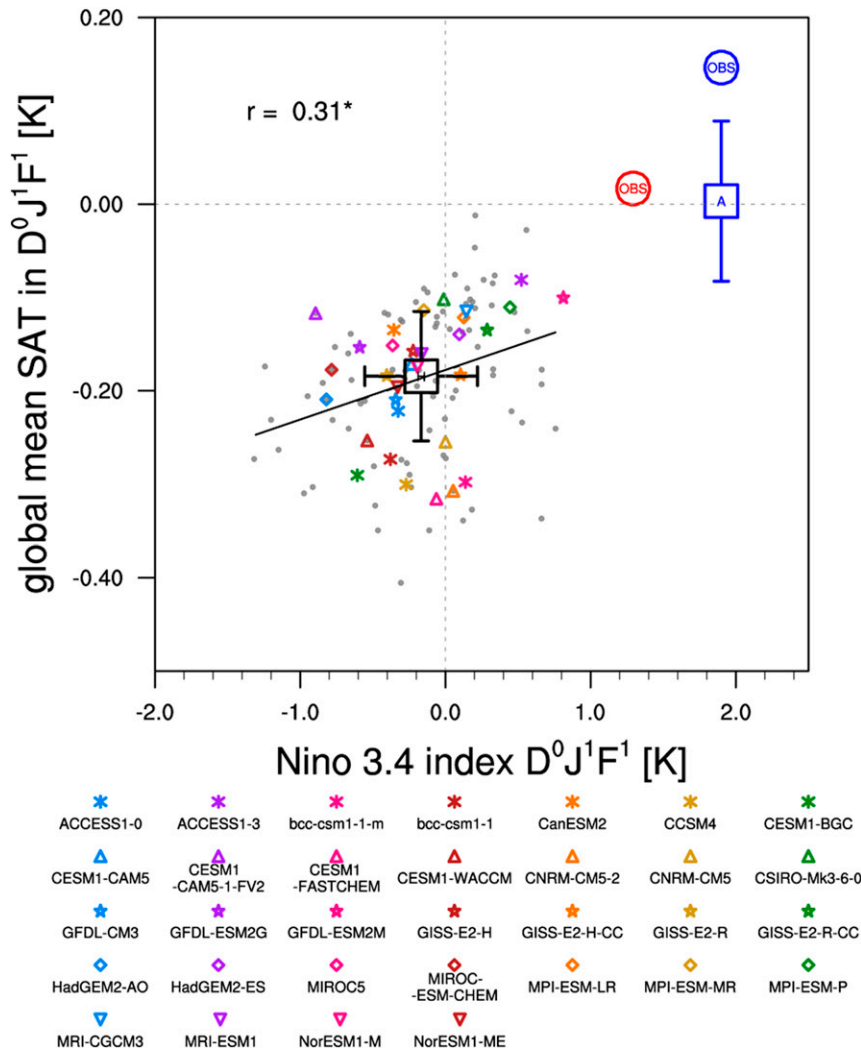


FIG. 4. Observed and simulated relationships between boreal-winter global mean SAT and Niño-3.4 index after the eruptions. Scatterplot of global mean SAT vs Niño-3.4 anomalies during the first boreal winter after the eruption. The red circle indicates the observational mean of the five eruptions from GISTEMP and ERSST, and the blue circle indicates the average for the latest two eruptions in observations. The large blue square indicates the AMIP MME mean for El Chichón and Pinatubo eruptions, and the black square indicates the historical MME mean for the five eruptions, with each bar denoting one standard deviation among the models. Small gray dots denote the composite of the five eruptions for each historical ensemble member, and small color symbols denote the associated ensemble mean of each model; also,  $r$  is the ensemble-to-ensemble correlation coefficient, and a single asterisk (\*) means significant values at the 95% confidence level according to Student's  $t$  test; “0” and “1” denote the eruption year and the year after the eruption, respectively.

eruptions although the SST field was specified. In the historical runs, this close relationship between global mean SAT and ENSO is also simulated, and the global mean SAT increases with the Niño-3.4 index at a ratio of 0.31, which is significant at the 95% confidence level. A few ensemble members, however, simulate the global cooling pause. The MME mean of the historical runs only replicates the neutral mode of ENSO and the

negative global mean SAT anomalies after the eruptions, which is significantly cooler than the observed El Niño and neutral global mean SAT anomalies. Even though some models with weak El Niño-like responses, such as GFDL-ESM2M and ACCESS1.3, simulate weaker global cooling than the others do, none captures the observed global cooling pause during the first boreal winter (Fig. 4).

The MME mean of the historical runs fails to show the El Niño-like response in the first boreal winter after the tropical eruptions (Fig. 2d). It has been found that the initial ocean condition (IOC), namely, the ENSO state in the pre-eruption winter, is important to the volcano–ENSO relationship (Ohba et al. 2013; Pausata et al. 2016; Predybaylo et al. 2017). No significant El Niño-like response can be found in the first boreal winter after an eruption if there is already an El Niño in the boreal winter before the eruption (Liu et al. 2018a). The Niño-3.4 index in the last boreal winter before the eruption was used as the IOC. To isolate El Niño from volcanic forcing, relative SST (Khodri et al. 2017) is employed here. In observations, the IOC of each eruption happened to be a La Niña or neutral state (Fig. 3a), the composite El Niño during the first boreal winter after the eruption is developed from a weak La Niña IOC, and an El Niño signal with westerly wind anomalies appears in the boreal summer and peaked in winter (Fig. 5a).

In the MME mean of the historical runs, there is no significant warming signal in the eastern equatorial Pacific in the first boreal winter after the eruptions (Fig. 5b). When the IOC is not in an El Niño state (Fig. 5c), the MME mean of the historical runs simulates the first-boreal-winter El Niño-like response that is significant in the central Pacific. However, the simulated response is much weaker than that in the observations, suggesting relatively weak air–sea interaction in these models. For an El Niño IOC (Fig. 5d), the response is determined by the evolution of El Niño, and a La Niña-like response is simulated in the first boreal winter, which is consistent with previous finding (Liu et al. 2018a; Predybaylo et al. 2017). Similar results can also be seen from large ensemble simulations of the CESM (Figs. 5f–h). The El Niño-like response in the first boreal winter after the eruptions is simulated with a La Niña or neutral IOC. In the CESM-LE, the El Niño-like response peaks in the second year after the eruptions.

In summary, the MME mean of the historical runs reproduces the El Niño-like response in the first boreal winter after the tropical eruptions when the IOC is not in an El Niño state, which is consistent with observations. The simulated El Niño-like response, however, is much weaker than that in the observations.

#### 4. Eurasian SAT and polar vortex responses

In the first boreal winter after each of the five tropical eruptions, a Eurasian warming occurred, which contributed to the pause in the 3-yr global cooling trend following the eruption (Fig. 2b). This Eurasian warming was also noted in previous works based on observations (Robock 2002; Robock and Mao 1992) and reconstructions (Fischer

et al. 2007). The Eurasian SAT has been found to be affected by the polar vortex, namely, a strong stratospheric polar vortex related to the NAO can induce significant Eurasian warming through planetary wave reflection and jet stream disturbance (Butler et al. 2014; Perlwitz and Graf 1995; Thompson and Wallace 2001). As shown in Fig. 6, the high correlation between Eurasian SAT and stratospheric polar vortex anomalies is found in both reanalysis datasets and the historical and AMIP runs of the CMIP5 models, which indicates that the CMIP5 models can simulate the polar vortex–Eurasian SAT relationship well.

Although the MME mean of the AMIP runs shows the first-boreal-winter global cooling pause after the eruption, this simulated global mean SAT is colder than that in observations (Fig. 4). The main reason is that the simulated Eurasian warming response in the AMIP runs is weaker than the observed one (Figs. 2b,c). The historical runs also fail to simulate the strong Eurasian warming response (Fig. 2d). The failure in reproducing the Eurasian warming response may result from poor simulation of stratospheric response, especially of the polar vortex (Driscoll et al. 2012).

Since the reanalysis of 20CRv2c only has assimilated surface observations (Compo et al. 2011), the reliability of its stratospheric variables is questionable. The reanalysis of polar vortex index is obtained from JRA-55 that starts in 1958. In the first boreal winter following each of the three eruptions after 1958, the observed Eurasian SAT anomaly was positive and was associated with an enhanced polar vortex (Fig. 7), which is consistent with previous findings (Zambri and Robock 2016). In both the historical and AMIP runs, the Eurasian SAT anomaly is significantly correlated to the anomalous polar vortex, with the correlations being 0.47 and 0.50, respectively; both are significant at the 95% confidence level (Figs. 7a,b). In the MME mean of the historical runs, the simulated Eurasian warming and polar vortex enhancement in the first boreal winter are significantly weaker compared to the observed ones (Fig. 7a). The strong polar vortex, exceeding 0.5 standard deviations of the reanalysis in the period of 1958–2005, is only simulated in HadGEM2-AO and the three NCAR models (CESM1-CAM5.1-FV2, CESM1-WACCM, and CESM1-BGC). Although each of these models has only one ensemble member, it may be good at representing stratospheric processes; the reason for this requires further study.

In the AMIP runs (Fig. 7b), which are forced by specified SST, only NorESM1-M, GFDL-HIRAM-C360, and two BCC models (BCC-CSM1.1-m and BCC-CSM1.1) simulate the strong polar vortex enhancement and Eurasian warming. It can be seen from the MME mean of the AMIP runs that the Eurasian warming and polar

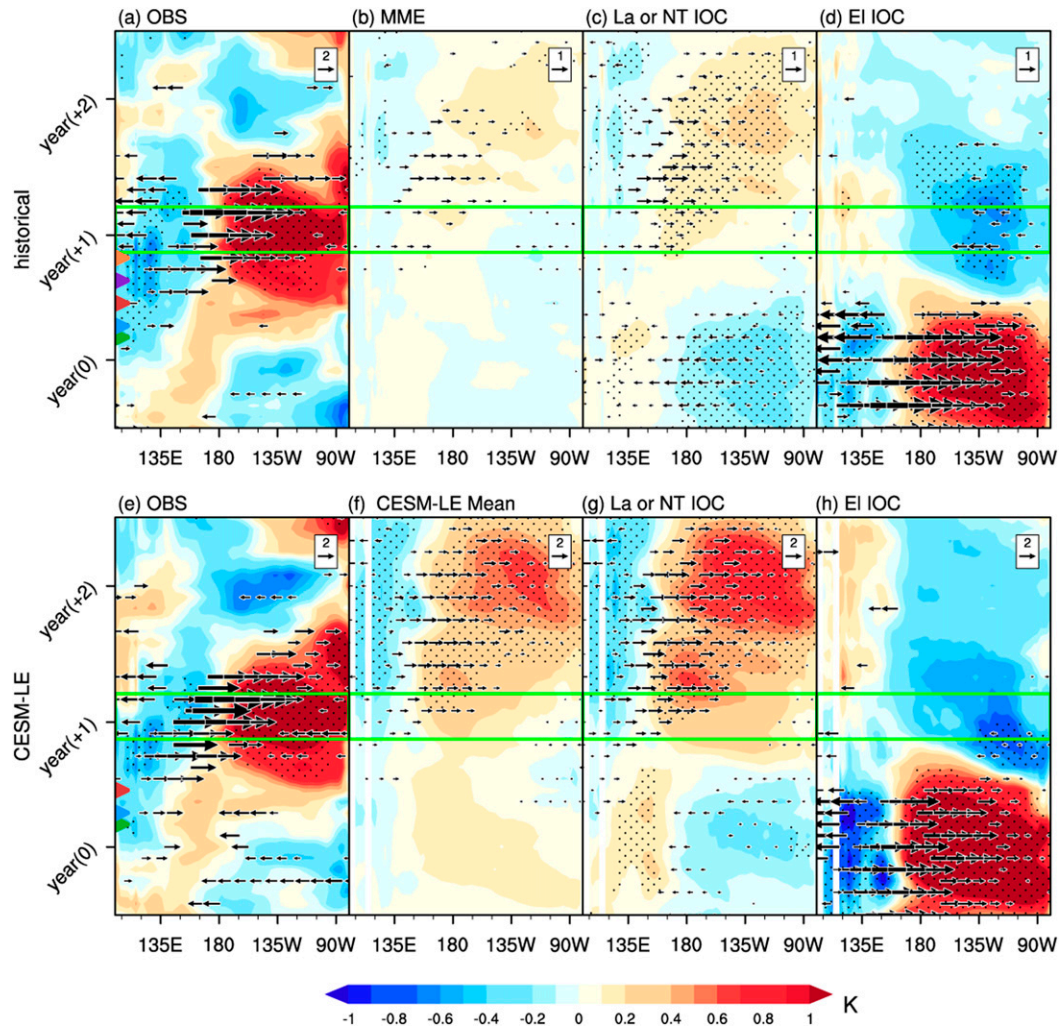


FIG. 5. Observed and simulated role of initial oceanic condition (IOC) in the volcano-ENSO relationship. Results for evolution of composite equatorial ( $5^{\circ}\text{S}$ – $5^{\circ}\text{N}$  average) relative SST anomalies (shading; K) and 850-hPa zonal wind anomalies (vector;  $\text{m s}^{-1}$ ) with respect to the five years preceding each eruption in (a) observations of ERSST and 20CRV2c and in the MME mean (b) of all historical runs, (c) of historical runs with a La Niña (LA) or neutral (NT) IOC, and (d) of the historical runs with an El Niño IOC. The El Niño IOC is defined when the IOC of the Niño-3.4 index is above 1.0 standard deviation. Green lines indicate the first boreal winter after the eruption. Stippling indicates SST anomaly significant at the 95% confidence level, which means that 22 of the 32 CMIP5 models agree on the sign of the anomaly. Only significant wind anomalies are drawn; “0” and “1” denote the eruption year and the year after the eruption, respectively. The triangles between year (0) and year (1) with the same color as in Fig. 1 represent the eruption times. (e)–(h) As in (a)–(d), but for the last three eruptions in observations and CESM-LE.

vortex enhancement are relatively weaker than those in the observations, which means that most models that participated in the AMIP runs underestimate the direct volcanic aerosol effect in enhancing the polar vortex.

Figure 8 shows the composite distribution of polar vortex responses in different reanalysis datasets and in CMIP5 simulations. In JRA-55 (Fig. 8a), a strong positive polar vortex anomaly was observed at 50 hPa during the first boreal winter after each of the three eruptions

since 1958. The center of the polar vortex anomaly was over the Arctic region. Due to the tropical warming and polar cooling in the stratosphere, strong westerly wind anomalies appeared near  $70^{\circ}\text{N}$  (Fig. 8b). All the three eruptions, namely, the Agung, El Chichón, and Pinatubo eruptions, were associated with similar polar vortices, but the polar vortex of the Pinatubo eruption was weakly increased. This strengthened polar vortex can also be seen in the ERA-40 reanalysis after the 1982 El

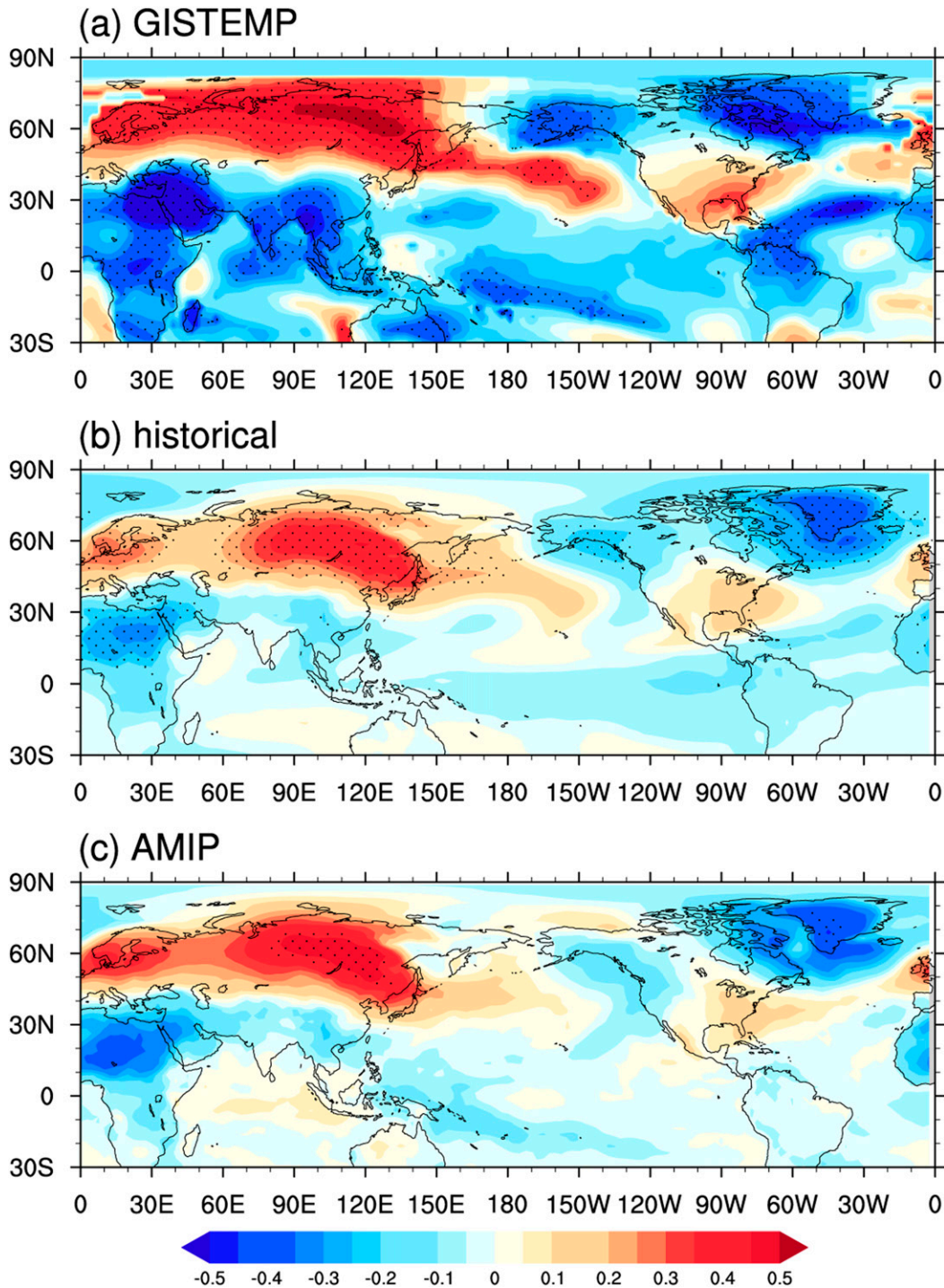


FIG. 6. Correlation between SAT and polar vortex in reanalysis and simulations. Shown is the correlation coefficient map of boreal-winter SAT anomalies with respect to boreal-winter polar vortex index anomalies in (a) GISTEMP from 1958 to 2014, (b) historical runs from 1870 to 2005, and (c) AMIP runs from 1979 to 2005. The annual cycle and the long-term linear trend are removed before the calculation of anomalies. Stippling indicates the anomaly significant above the 95% confidence level based on Student's *t* test.

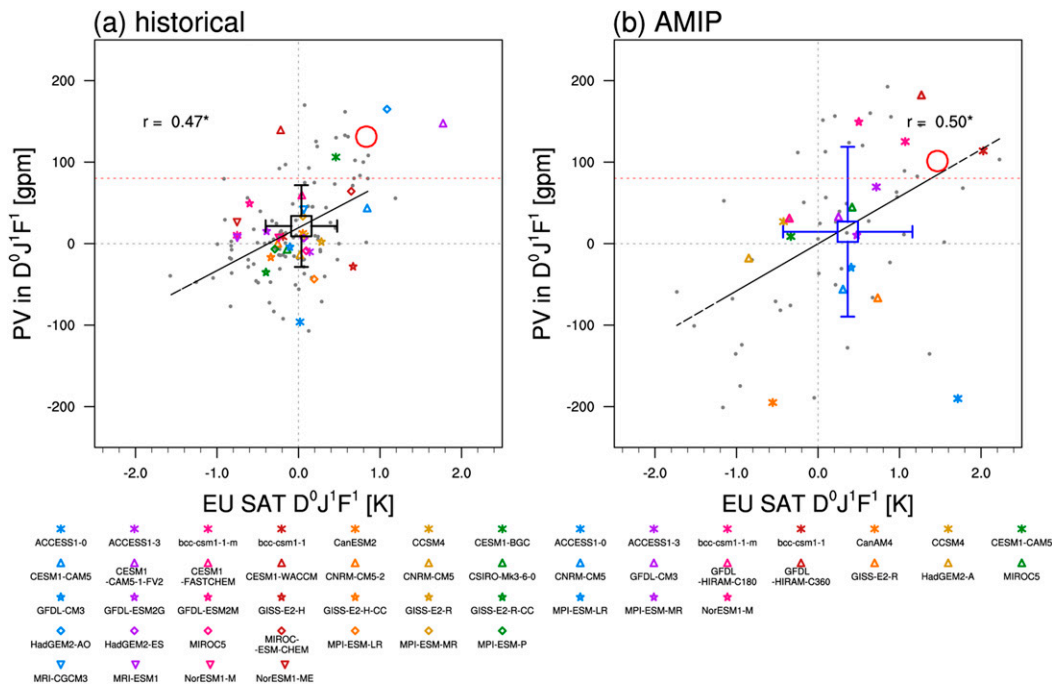


FIG. 7. Observed and simulated relationships between boreal-winter polar vortex and Eurasian SAT after the eruptions. Scatterplot of polar vortex index vs Eurasian ( $40^{\circ}$ – $80^{\circ}$ N,  $0^{\circ}$ – $150^{\circ}$ E) SAT anomalies during the first boreal winter after the eruption in (a) historical runs and (b) AMIP runs since 1958. The large red circles denote the average of observations or reanalysis, and the large square denotes the MME mean in historical runs (black) and AMIP runs (blue) with the bars indicating one standard deviation among the models. The red dashed line is the threshold of relative strong polar vortex response, which is 0.5 standard deviations of reanalysis during the studied period. The small gray dot denotes the composite of the eruptions for each ensemble member, and small color symbols denote ensemble mean of each model. Also,  $r$  is the ensemble-to-ensemble correlation coefficient, and a single asterisk (\*) means significant values at 95% confidence level according to Student's  $t$  test; “0” and “1” denote the eruption year and the year after the eruption, respectively.

Chichón and 1991 Pinatubo eruptions (Zambri and Robock 2016) and in the NCEP reanalysis during the two posteruption winters (Graf et al. 2014). Compared to the result based on JRA-55, the positive polar vortex anomaly in the first boreal winter after the eruption in 20CRv2c is very weak, and no significant anomalous geopotential height and temperature signals can be detected over the polar stratosphere (Figs. 8c,d). Without assimilation of upper-level variables, the NCEP Global Forecast System model used for 20CRv2c still has difficulty in capturing observed volcano-induced polar vortex change.

In the MME mean of the AMIP runs (Fig. 8e), the polar vortex anomaly is very weak, and a dipole pattern after the eruption is simulated with significant positive geopotential height anomaly over Alaska and weak negative anomaly over the Greenland Sea, which is not consistent with the results based on JRA-55 (Fig. 8a). The historical runs suffer the same problem (Fig. 8g). Although the warming signal in the tropical stratosphere is simulated, the polar vortex is not enhanced significantly

and the westerly anomalies around the North Pole are much weaker than those based on JRA-55 (Figs. 8f,h), which means the direct volcanic aerosol effect on enhancing the polar vortex is underestimated in the CMIP5 models. The strength of volcanic forcing should be large enough to detect the significant polar vortex response (Bittner et al. 2016). Our results based on the strong 1883 Krakatau and 1991 Pinatubo eruptions also showed that the response of the polar vortex is underestimated in the historical runs of the CMIP5 models (not shown).

For all of these 32 CMIP5 models, when a strong response is defined by exceeding 0.5 standard deviations of observations or reanalysis, none of them, either with a La Niña or neutral IOC, simulate the observed El Niño and strong positive polar vortex anomalies at the same time in the first boreal winter after the tropical eruption (Fig. 9). Among the 97 ensemble members of these 32 models, only four ensemble members simulate El Niño and strong positive polar vortex anomalies simultaneously.

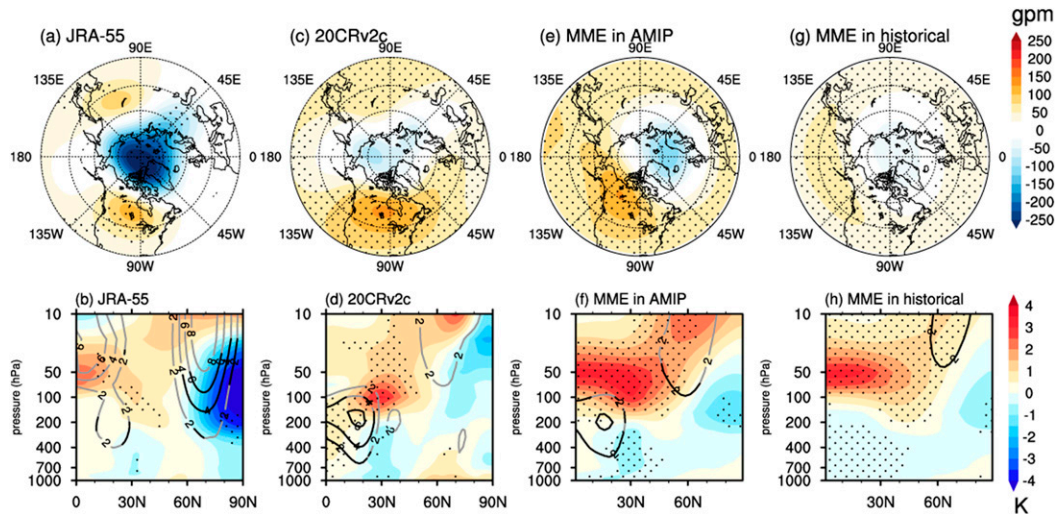


FIG. 8. Boreal winter polar vortex and stratospheric anomalies after the eruptions in reanalysis and simulations. Composite 50-hPa geopotential height anomalies (shading; gpm) with respect to the five years preceding each eruption during the first boreal winter after the eruption in (a) JRA-55, (c) 20CRv2c, (e) the MME mean of AMIP runs, and (g) the MME mean of historical runs since 1958. (b),(d),(f),(h) The composites of zonal-mean temperature (shading; K) and zonal wind (contour;  $\text{m s}^{-1}$ ) anomalies as a function of latitude and height. Stippling indicates anomalies significant at the 95% confidence level, which means more than 13 of the 17 AMIP models and more than 22 of the 32 CMIP5 models of historical runs agree on the sign of the anomaly. Contour interval is  $2 \text{ m s}^{-1}$ , and significant zonal wind anomalies are drawn in black.

In summary, the stratospheric polar vortex is mainly affected by direct volcanic aerosol-induced stratospheric warming in the reanalysis. Despite being reproduced by both the historical and AMIP runs of the CMIP5 models, the enhanced polar vortex in the first boreal winter after the eruption is very weak compared to that based on the reanalysis. Not only the CMIP5 models but also the NCEP Global Forecast System model underestimates the direct volcanic aerosol effect, and neither of them adequately captures the role of volcanic forcing in changing the polar vortex, which are consistent with previous findings (Marshall et al. 2009). Because a higher stratospheric resolution does not increase a model's ability to simulate the response to volcanic forcing (Charlton-Perez et al. 2013; Marshall et al. 2009), deficient nonlinear stratosphere–troposphere interaction (Stenchikov et al. 2006) may explain these models' limitation.

## 5. Discussion on internal variability–induced global cooling pause

We cannot conclude that this global cooling pause is totally excited by tropical eruptions only based on these five samples, because internal variability may be a potential cause (Polvani et al. 2019). Forty-one ensemble members of the CESM-LE are thus analyzed for the latest three eruptions since 1920 to address this question.

The significant linear relationship between global mean SAT and Niño-3.4 index anomalies and that between the polar vortex and Eurasian SAT anomalies are simulated by the 41 ensemble members of the CESM-LE, with correlation coefficients being 0.76 and 0.54, respectively; both are significant at the 95% confidence level (Fig. 10). The simulated global mean SAT and Niño-3.4 index anomalies in the ensemble mean of the CESM-LE in the first boreal winter are  $-0.13$  and  $0.12$  K, respectively (Fig. 10a), which are much colder than the observations, although they are warmer than those simulated by the CMIP5 historical runs (Fig. 4). The simulated polar vortex enhancement and Eurasian warming in the ensemble mean are also much weaker than the observed ones (Fig. 10b).

Among these 41 ensemble members of the CESM-LE, four simulate significant global cooling pause as well as El Niño responses (Fig. 10a), and other four replicate significant polar vortex enhancement and Eurasian warming (Fig. 10b), which exceed 0.5 standard deviation of observations or reanalysis. For the ensemble mean of the CESM-LE (Fig. 11a), tropical cooling is reproduced, but the central equatorial Pacific warming is weak. Significant warming is only simulated over the Arctic region (Fig. 11a), and the polar vortex enhancement is weak (Fig. 11b). Ensemble members that simulate the global cooling pause reproduce SAT responses similar to those in observations except that the Eurasian warming is shifted northward (Fig. 11c), but they fail to simulate

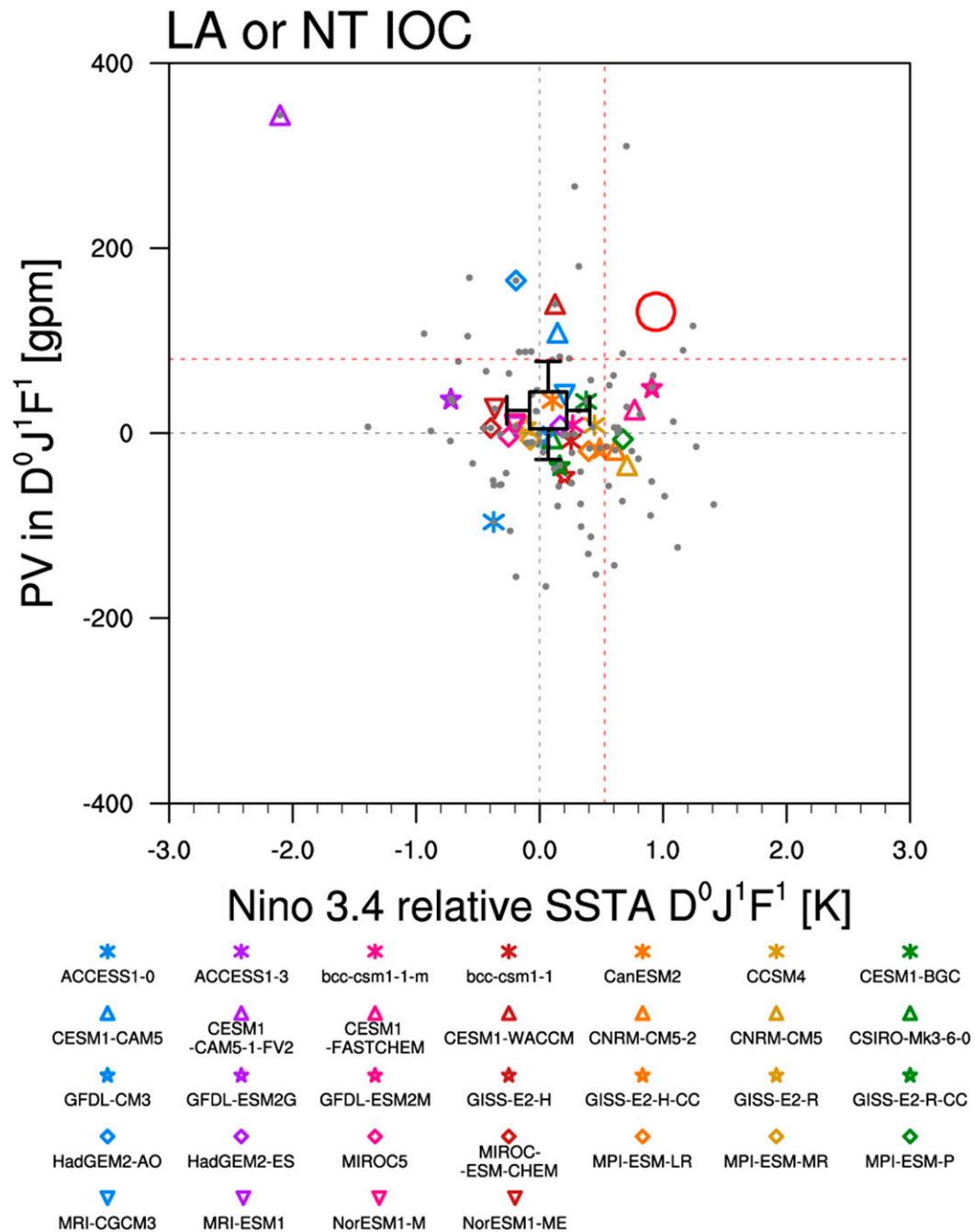


FIG. 9. Simulated polar vortex and ENSO responses in the first boreal winter after the tropical eruptions. Shown in the scatterplot is polar vortex vs Niño-3.4 relative SST anomalies during the first winter after the eruption with La Niña or neutral IOC since 1958. The red circle indicates the average of observations or reanalysis. The black square indicates the MME mean of the historical runs, with the bar denoting one standard deviation among the models. The red dashed line is the threshold of relative strong responses, which is 0.5 standard deviation of observations or reanalysis during the studied period. The small gray dot denotes the composite of the five eruptions for each historical ensemble member, and small color symbols denote the associated ensemble mean of each model; “0” and “1” denote the eruption year and the year after the eruption, respectively.

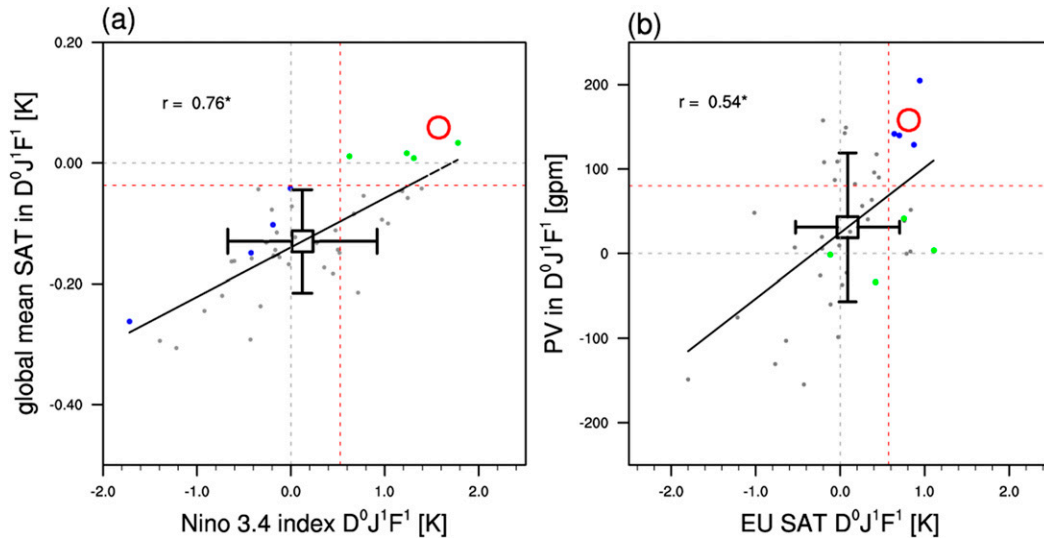


FIG. 10. Simulated SAT responses in CESM-LE. (a) Scatterplot of global mean SAT vs Niño-3.4 anomalies during the first boreal winter after the 1963, 1982, and 1991 eruptions. The red circle indicates the observational mean of these three eruptions from GISTEMP and ERSST. The black square indicates the ensemble mean of CESM-LE, with each bar denoting one standard deviation among the ensemble. Small gray dots denote the composite of the three eruptions for each ensemble member. Ensemble members simulating global cooling pause with El Niño responses are in green and ensemble members simulating enhanced polar vortex with Eurasian warming are in blue. The red dashed line is the threshold of relatively strong responses, which is 0.5 standard deviations of observations or reanalysis during the studied period. For the global mean SAT, the red horizontal dashed line has a distance of 0.5 standard deviations of observations with observed mean. Also,  $r$  is the ensemble-to-ensemble correlation coefficient, and a single asterisk (\*) means significant values at 95% confidence level according to Student's  $t$  test; "0" and "1" denote the eruption year and the year after the eruption, respectively. (b) As in (a), but showing a scatterplot of the polar vortex index vs Eurasian SAT anomalies.

strong polar vortex enhancement (Fig. 11d). For the ensemble members that capture strong polar vortex enhancement and Eurasian warming (Figs. 11e and 8f), the global cooling pause, however, is not simulated, especially over the tropics (Fig. 11e).

The ensemble mean of the CESM-LE fails to show the global cooling pause; also, the simulated polar vortex enhancement and Eurasian warming are very weak. Although some ensemble members capture the global cooling pause or polar vortex enhancement, they do not simulate both well.

Whether the global cooling pause in the first boreal winter is a response to a tropical eruption or is internal variability is still an open question. Strong polar vortex enhancement in reanalysis data is argued to result from internal variability (Bittner et al. 2016; Polvani et al. 2019). We conclude that the global cooling pause is a response to the tropical eruption based on long-term reconstruction evidence that shows a significant El Niño response (Adams et al. 2003; Liu et al. 2018a,b) and a significant overall warm anomaly over northern Europe (Fischer et al. 2007) in the first boreal winter after the tropical eruption, and based on physical processes reviewed in the introduction, including the

dynamic thermostat mechanism and the temperature gradient mechanism.

## 6. Conclusions

In this study, we investigated global SAT responses during the first boreal winter after the five major tropical volcanic eruptions since 1870 compared simulations of CMIP5 historical and AMIP runs and of CESM-LE to observations and reanalysis. In observations, the global cooling pause, which is due to tropical El Niño-like warming and Eurasian warming, is seen during the first posteruption boreal winter, thereby forming a deviation from the 3-yr global cooling trend after the tropical eruptions. Direct volcanic aerosol-induced warming in the tropical lower stratosphere and cooling in the polar stratosphere increase the meridional temperature gradient and enhance the stratospheric polar vortex, resulting in strong Eurasian surface warming (Figs. 8a,b).

In the AMIP runs, the first-boreal-winter global cooling pause is simulated with specified SST forcing. In the historical runs, a monotonous global cooling trend rather than a global cooling pause is produced. The IOC is one key to simulate the first-boreal-winter El Niño response,

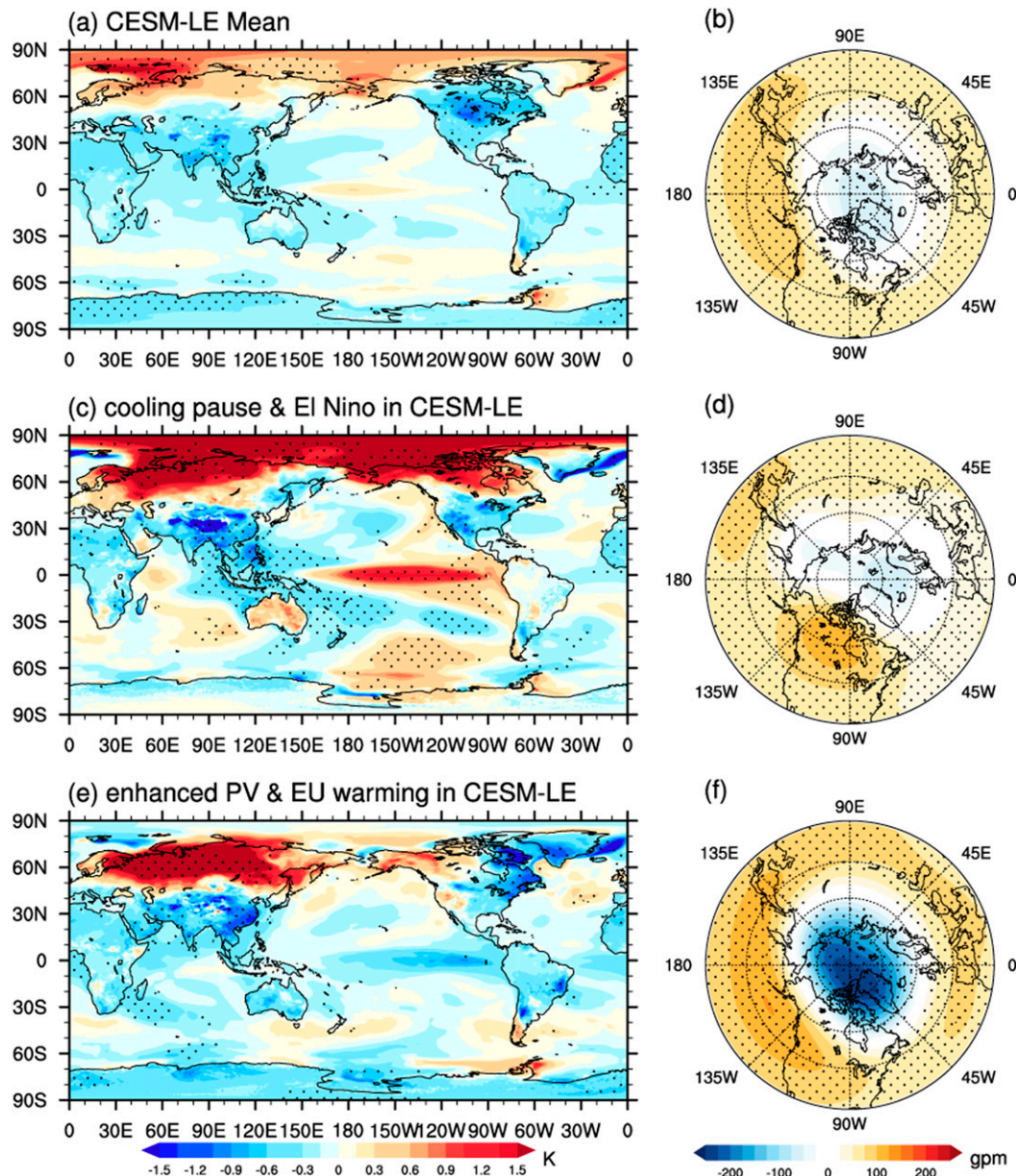


FIG. 11. Internal variability-induced global cooling pause. Composite (a) SAT anomalies (shading; K) and (b) 50-hPa geopotential height anomalies (shading; gpm) with respect to the five years preceding each eruption during the first boreal winter after the 1963, 1982, and 1991 eruptions. Stippling indicates anomalies significant at the 95% confidence level. (c),(d) As in (a),(b), but for selected ensemble members that simulate the global cooling pause and El Niño response. (e),(f) The ensemble members simulating the polar vortex enhancement and Eurasian warming.

as the latter is reproduced when the pre-eruption IOC is not in an El Niño state, but tropical cooling is still produced since the simulated El Niño response is very weak compared to that in the observations. Although the CMIP5 models show the Eurasian SAT response to the polar vortex (Fig. 6), the simulated Eurasian warming and positive stratospheric polar vortex responses to the eruptions are very weak in both AMIP and historical runs (Fig. 8), which means that the

CMIP5 models underestimate the direct volcanic aerosol effect on the stratosphere. The majority of the CMIP5 coupled models cannot simulate both El Niño and enhanced polar vortex responses (Fig. 9). The abovementioned processes controlling the global cooling pause in the first post-eruption boreal winter are summarized in Fig. 12. Although this global cooling pause is simulated by some ensemble members of the CESM-LE as an internal mode (Figs. 10 and 11),

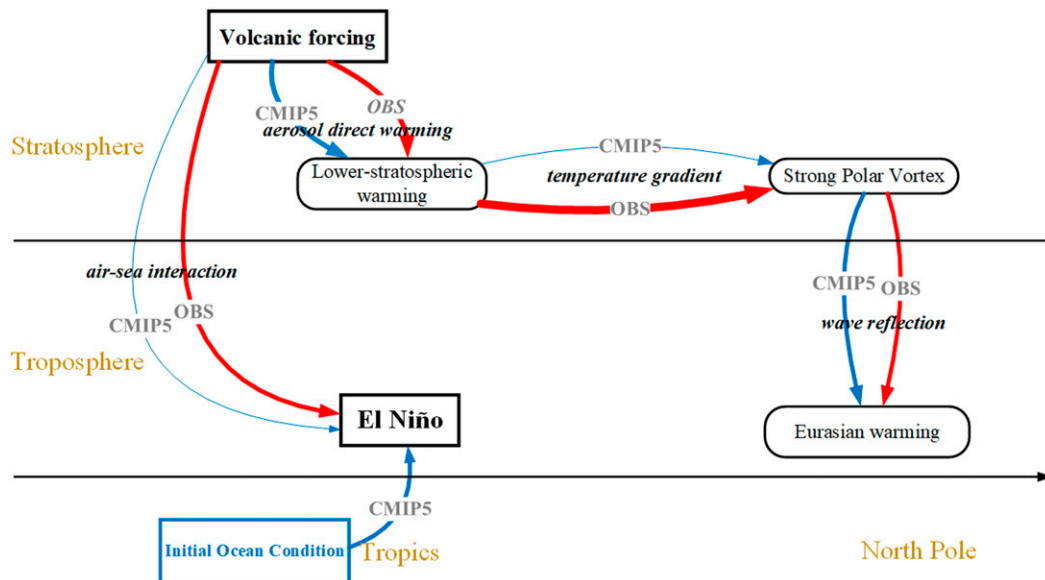


FIG. 12. Schematic diagram showing El Niño and direct volcanic aerosol effects under volcano forcing, and possible mechanisms. The red and blue vectors represent the observations and CMIP5 simulations, respectively. The relative strength of the effect is represented by vector width; a thicker vector denotes a stronger effect.

we conclude that it is a response to tropical volcanic eruption according to the reconstruction analysis.

Different from the observations, the models fail to simulate the first-boreal-winter El Niño after a tropical eruption (Fig. 5). This suggests that the CMIP5 models underestimate the role of the thermostat mechanism (Clement et al. 1996) or the Bjerknes feedback (Bjerknes 1969) in exciting El Niño response. Neither the CMIP5 models nor the NCEP Global Forecast System model used for 20CRv2c can simulate the strong polar vortex in the first boreal winter after a tropical eruption. All these deficiencies in simulating global SAT responses to the tropical eruptions call for urgent improvement of models; and the upcoming model intercomparison project on the climate response to volcanic forcing (VolMIP; Zanchettin et al. 2016) offers a good opportunity to discuss these deficiencies. Analysis of climate responses to large volcanic eruptions provides an additional perspective to evaluate our models' sensitivity to external forcing.

**Acknowledgments.** This work is supported by the Natural Science Foundation of China (41975107), the Public Science and Technology Research Funds Projects of Ocean (201505013), the National Science Foundation of the United States (AGS-1540783), the National Natural Science Foundation of China (41971108), and the Strategic Priority Research Program of Chinese Academy of Sciences (XDA20060401). We acknowledge the World Climate Research Programme's Working Group on Coupled Modelling, which is responsible for CMIP,

and we thank the climate modeling groups for producing and making available their model outputs. This paper is ESMC Contribution No. 297.

## REFERENCES

- Adams, J. B., M. E. Mann, and C. M. Ammann, 2003: Proxy evidence for an El Niño-like response to volcanic forcing. *Nature*, **426**, 274–278, <https://doi.org/10.1038/nature02101>.
- Ammann, C. M., G. A. Meehl, W. M. Washington, and C. S. Zender, 2003: A monthly and latitudinally varying volcanic forcing dataset in simulations of 20th century climate. *Geophys. Res. Lett.*, **30**, 1657, <https://doi.org/10.1029/2003GL016875>.
- , F. Joos, D. S. Schimel, B. L. Otto-Bliesner, and R. A. Tomas, 2007: Solar influence on climate during the past millennium: Results from transient simulations with the NCAR Climate System Model. *Proc. Natl. Acad. Sci. USA*, **104**, 3713–3718, <https://doi.org/10.1073/pnas.0605064103>.
- Andres, R. J., and A. D. Kasgnoc, 1998: A time-averaged inventory of subaerial volcanic sulfur emissions. *J. Geophys. Res.*, **103**, 25 251–25 261, <https://doi.org/10.1029/98JD02091>.
- Angell, J. K., 1988: Impact of El Niño on the delineation of tropospheric cooling due to volcanic eruptions. *J. Geophys. Res.*, **93**, 3697–3704, <https://doi.org/10.1029/JD093iD04p03697>.
- Barnes, E. A., S. Solomon, and L. M. Polvani, 2016: Robust wind and precipitation responses to the Mount Pinatubo eruption, as simulated in the CMIP5 models. *J. Climate*, **29**, 4763–4778, <https://doi.org/10.1175/JCLI-D-15-0658.1>.
- Bentsen, M., and Coauthors, 2013: The Norwegian Earth System Model, NorESM1-M—Part 1: Description and basic evaluation of the physical climate. *Geosci. Model Dev.*, **6**, 687–720, <https://doi.org/10.5194/gmd-6-687-2013>.
- Bi, D. H., and Coauthors, 2013: The ACCESS coupled model: Description, control climate and evaluation. *Aust. Meteor. Oceanogr. J.*, **63**, 41–64, <https://doi.org/10.22499/2.6301.004>.

- Bittner, M., H. Schmidt, C. Timmreck, and F. Sienz, 2016: Using a large ensemble of simulations to assess the Northern Hemisphere stratospheric dynamical response to tropical volcanic eruptions and its uncertainty. *Geophys. Res. Lett.*, **43**, 9324–9332, <https://doi.org/10.1002/2016GL070587>.
- Bjerknes, J., 1969: Atmospheric teleconnections from the equatorial Pacific. *Mon. Wea. Rev.*, **97**, 163–172, [https://doi.org/10.1175/1520-0493\(1969\)097<0163:ATFTEP>2.3.CO;2](https://doi.org/10.1175/1520-0493(1969)097<0163:ATFTEP>2.3.CO;2).
- Butler, A. H., L. M. Polvani, and C. Deser, 2014: Separating the stratospheric and tropospheric pathways of El Niño–Southern Oscillation teleconnections. *Environ. Res. Lett.*, **9**, 024014, <https://doi.org/10.1088/1748-9326/9/2/024014>.
- Charlton-Perez, A. J., and Coauthors, 2013: On the lack of stratospheric dynamical variability in low-top versions of the CMIP5 models. *J. Geophys. Res. Atmos.*, **118**, 2494–2505, <https://doi.org/10.1002/JGRD.50125>.
- Chylek, P., J. Li, M. K. Dubey, M. Wang, and G. Lesins, 2011: Observed and model simulated 20th century Arctic temperature variability: Canadian Earth System Model CanESM2. *Atmos. Chem. Phys. Discuss.*, **11**, 22 893–22 907, <https://doi.org/10.5194/acpd-11-22893-2011>.
- Clement, A. C., R. Seager, M. A. Cane, and S. E. Zebiak, 1996: An ocean dynamical thermostat. *J. Climate*, **9**, 2190–2196, [https://doi.org/10.1175/1520-0442\(1996\)009<2190:AODT>2.0.CO;2](https://doi.org/10.1175/1520-0442(1996)009<2190:AODT>2.0.CO;2).
- Compo, G. P., and Coauthors, 2011: The Twentieth Century Reanalysis project. *Quart. J. Roy. Meteor. Soc.*, **137**, 1–28, <https://doi.org/10.1002/qj.776>.
- Crowley, T. J., 2000: Causes of climate change over the past 1000 years. *Science*, **289**, 270–277, <https://doi.org/10.1126/science.289.5477.270>.
- Ding, Y. N., J. A. Carton, G. A. Chepurin, G. Stenchikov, A. Robock, L. T. Sentman, and J. P. Krasting, 2014: Ocean response to volcanic eruptions in Coupled Model Intercomparison Project 5 simulations. *J. Geophys. Res. Oceans*, **119**, 5622–5637, <https://doi.org/10.1002/2013JC009780>.
- Donner, L. J., and Coauthors, 2011: The dynamical core, physical parameterizations, and basic simulation characteristics of the atmospheric component AM3 of the GFDL global coupled model CM3. *J. Climate*, **24**, 3484–3519, <https://doi.org/10.1175/2011JCLI3955.1>.
- Driscoll, S., A. Bozzo, L. J. Gray, A. Robock, and G. Stenchikov, 2012: Coupled Model Intercomparison Project 5 (CMIP5) simulations of climate following volcanic eruptions. *J. Geophys. Res.*, **117**, D17105, <https://doi.org/10.1029/2012JD017607>.
- Dunne, J. P., and Coauthors, 2012: GFDL's ESM2 global coupled climate–carbon Earth system models. Part I: Physical formulation and baseline simulation characteristics. *J. Climate*, **25**, 6646–6665, <https://doi.org/10.1175/JCLI-D-11-00560.1>.
- Fischer, E. M., J. Luterbacher, E. Zorita, S. F. B. Tett, C. Casty, and H. Wanner, 2007: European climate response to tropical volcanic eruptions over the last half millennium. *Geophys. Res. Lett.*, **34**, L05707, <https://doi.org/10.1029/2006GL027992>.
- Gao, C. C., A. Robock, and C. Ammann, 2008: Volcanic forcing of climate over the past 1500 years: An improved ice core-based index for climate models. *J. Geophys. Res.*, **113**, D16112, <https://doi.org/10.1029/2008JD010239>.
- Gent, P. R., and Coauthors, 2011: The Community Climate System Model version 4. *J. Climate*, **24**, 4973–4991, <https://doi.org/10.1175/2011JCLI4083.1>.
- Giorgetta, M. A., and Coauthors, 2013: Climate and carbon cycle changes from 1850 to 2100 in MPI-ESM simulations for the Coupled Model Intercomparison Project phase 5. *J. Adv. Model. Earth Syst.*, **5**, 572–597, <https://doi.org/10.1002/jame.20038>.
- Graf, H. F., Q. Li, and M. A. Giorgetta, 2007: Volcanic effects on climate: Revisiting the mechanisms. *Atmos. Chem. Phys.*, **7**, 4503–4511, <https://doi.org/10.5194/acp-7-4503-2007>.
- , D. Zanchettin, C. Timmreck, and M. Bittner, 2014: Observational constraints on the tropospheric and near-surface winter signature of the Northern Hemisphere stratospheric polar vortex. *Climate Dyn.*, **43**, 3245–3266, <https://doi.org/10.1007/s00382-014-2101-0>.
- Gu, G. J., and R. F. Adler, 2011: Precipitation and temperature variations on the interannual time scale: Assessing the impact of ENSO and volcanic eruptions. *J. Climate*, **24**, 2258–2270, <https://doi.org/10.1175/2010JCLI3727.1>.
- Hegerl, G. C., T. J. Crowley, S. K. Baum, K.-Y. Kim, and W. T. Hyde, 2003: Detection of volcanic, solar and greenhouse gas signals in paleo-reconstructions of Northern Hemispheric temperature. *Geophys. Res. Lett.*, **30**, 1242, <https://doi.org/10.1029/2002GL016635>.
- Huang, B. Y., and Coauthors, 2017: Extended Reconstructed Sea Surface Temperature, version 5 (ERSSTv5): Upgrades, validations, and intercomparisons. *J. Climate*, **30**, 8179–8205, <https://doi.org/10.1175/JCLI-D-16-0836.1>.
- Hurrell, J. W., and Coauthors, 2013: The Community Earth System Model: A framework for collaborative research. *Bull. Amer. Meteor. Soc.*, **94**, 1339–1360, <https://doi.org/10.1175/BAMS-D-12-00121.1>.
- Kay, J. E., and Coauthors, 2015: The Community Earth System Model (CESM) large ensemble project: A community resource for studying climate change in the presence of internal climate variability. *Bull. Amer. Meteor. Soc.*, **96**, 1333–1349, <https://doi.org/10.1175/BAMS-D-13-00255.1>.
- Khodri, M., and Coauthors, 2017: Tropical explosive volcanic eruptions can trigger El Niño by cooling tropical Africa. *Nat. Commun.*, **8**, 778, <https://doi.org/10.1038/s41467-017-00755-6>.
- Kobayashi, S., and Coauthors, 2015: The JRA-55 reanalysis: General specifications and basic characteristics. *J. Meteor. Soc. Japan*, **93**, 5–48, <https://doi.org/10.2151/jmsj.2015-001>.
- Lehner, F., A. P. Schurer, G. C. Hegerl, C. Deser, and T. L. Frölicher, 2016: The importance of ENSO phase during volcanic eruptions for detection and attribution. *Geophys. Res. Lett.*, **43**, 2851–2858, <https://doi.org/10.1002/2016GL067935>.
- Lenssen, N. J. L., G. A. Schmidt, J. E. Hansen, M. J. Menne, A. Persin, R. Ruedy, and D. Zyss, 2019: Improvements in the GISTEMP uncertainty model. *J. Geophys. Res. Atmos.*, **124**, 6307–6326, <https://doi.org/10.1029/2018JD029522>.
- Liu, F., C. Xing, L. Sun, B. Wang, D. Chen, and J. Liu, 2018a: How do tropical, Northern Hemispheric, and Southern Hemispheric volcanic eruptions affect ENSO under different initial ocean conditions? *Geophys. Res. Lett.*, **45**, 13 041–13 049, <https://doi.org/10.1029/2018GL080315>.
- , J. Li, B. Wang, J. Liu, T. Li, G. Huang, and Z. Wang, 2018b: Divergent El Niño responses to volcanic eruptions at different latitudes over the past millennium. *Climate Dyn.*, **50**, 3799–3812, <https://doi.org/10.1007/s00382-017-3846-z>.
- Maher, N., S. McGregor, M. H. England, and A. Sen Gupta, 2015: Effects of volcanism on tropical variability. *Geophys. Res. Lett.*, **42**, 6024–6033, <https://doi.org/10.1002/2015GL064751>.
- , D. Matei, S. Milinski, and J. Marotzke, 2018: ENSO change in climate projections: Forced response or internal variability? *Geophys. Res. Lett.*, **45**, 11 390–11 398, <https://doi.org/10.1029/2018GL079764>.

- Mann, M. E., R. S. Bradley, and M. K. Hughes, 1998: Global-scale temperature patterns and climate forcing over the past six centuries. *Nature*, **392**, 779–787, <https://doi.org/10.1038/33859>.
- , M. A. Cane, S. E. Zebiak, and A. Clement, 2005: Volcanic and solar forcing of the tropical Pacific over the past 1000 years. *J. Climate*, **18**, 447–456, <https://doi.org/10.1175/JCLI-3276.1>.
- Marshall, A. G., A. A. Scaife, and S. Ineson, 2009: Enhanced seasonal prediction of European winter warming following volcanic eruptions. *J. Climate*, **22**, 6168–6180, <https://doi.org/10.1175/2009JCLI3145.1>.
- Martin, G. M., and Coauthors, 2011: The HadGEM2 family of Met Office Unified Model climate configurations. *Geosci. Model Dev.*, **4**, 723–757, <https://doi.org/10.5194/gmd-4-723-2011>.
- McGregor, S., and A. Timmermann, 2011: The effect of explosive tropical volcanism on ENSO. *J. Climate*, **24**, 2178–2191, <https://doi.org/10.1175/2010JCLI3990.1>.
- Morice, C. P., J. J. Kennedy, N. A. Rayner, and P. D. Jones, 2012: Quantifying uncertainties in global and regional temperature change using an ensemble of observational estimates: The HadCRUT4 data set. *J. Geophys. Res.*, **117**, D08101, <https://doi.org/10.1029/2011JD017187>.
- Neale, R. B., and Coauthors, 2010: Description of the NCAR Community Atmosphere Model (CAM 5.0). NCAR Tech. Note NCAR/TN-486+STR, 268 pp., [www.cesm.ucar.edu/models/cesm1.1/cam/docs/description/cam5\\_desc.pdf](http://www.cesm.ucar.edu/models/cesm1.1/cam/docs/description/cam5_desc.pdf).
- Newhall, C. G., and S. Self, 1982: The Volcanic Explosivity Index (VEI) an estimate of explosive magnitude for historical volcanism. *J. Geophys. Res.*, **87**, 1231–1238, <https://doi.org/10.1029/JC087iC02p01231>.
- Nicholls, N., 1988: Low latitude volcanic eruptions and the El Niño–Southern Oscillation. *J. Climatol.*, **8**, 91–95, <https://doi.org/10.1002/joc.3370080109>.
- Ohba, M., H. Shiogama, T. Yokohata, and M. Watanabe, 2013: Impact of strong tropical volcanic eruptions on ENSO simulated in a coupled GCM. *J. Climate*, **26**, 5169–5182, <https://doi.org/10.1175/JCLI-D-12-00471.1>.
- Oppenheimer, C., 2003: Climatic, environmental and human consequences of the largest known historic eruption: Tambora volcano (Indonesia) 1815. *Prog. Phys. Geogr. Earth Environ.*, **27**, 230–259, <https://doi.org/10.1191/0309133303pp379ra>.
- Paik, S., and S.-K. Min, 2016: Climate responses to volcanic eruptions assessed from observations and CMIP5 multi-models. *Climate Dyn.*, **48**, 1017–1030, <https://doi.org/10.1007/s00382-016-3125-4>.
- Pausata, F. S. R., C. Karamperidou, R. Caballero, and D. S. Battisti, 2016: ENSO response to high-latitude volcanic eruptions in the Northern Hemisphere: The role of the initial conditions. *Geophys. Res. Lett.*, **43**, 8694–8702, <https://doi.org/10.1002/2016GL069575>.
- Perlwitz, J., and H.-F. Graf, 1995: The statistical connection between tropospheric and stratospheric circulation of the Northern Hemisphere in winter. *J. Climate*, **8**, 2281–2295, [https://doi.org/10.1175/1520-0442\(1995\)008<2281:TSCBTA>2.0.CO;2](https://doi.org/10.1175/1520-0442(1995)008<2281:TSCBTA>2.0.CO;2).
- , and N. Harnik, 2003: Observational evidence of a stratospheric influence on the troposphere by planetary wave reflection. *J. Climate*, **16**, 3011–3026, [https://doi.org/10.1175/1520-0442\(2003\)016<3011:OEOASI>2.0.CO;2](https://doi.org/10.1175/1520-0442(2003)016<3011:OEOASI>2.0.CO;2).
- Polvani, L. M., A. Banerjee, and A. Schmidt, 2019: Northern Hemisphere continental winter warming following the 1991 Mt. Pinatubo eruption: Reconciling models and observations. *Atmos. Chem. Phys.*, **19**, 6351–6366, <https://doi.org/10.5194/ACP-19-6351-2019>.
- Predybaylo, E., G. L. Stenchikov, A. T. Wittenberg, and F. Zeng, 2017: Impacts of a Pinatubo-size volcanic eruption on ENSO. *J. Geophys. Res. Atmos.*, **122**, 925–947, <https://doi.org/10.1002/2016JD025796>.
- Rayner, N. A., D. E. Parker, E. B. Horton, C. K. Folland, L. V. Alexander, D. P. Rowell, E. C. Kent, and A. Kaplan, 2003: Global analyses of sea surface temperature, sea ice, and night marine air temperature since the late nineteenth century. *J. Geophys. Res.*, **108**, 4407, <https://doi.org/10.1029/2002JD002670>.
- , P. Brohan, D. E. Parker, C. K. Folland, J. J. Kennedy, M. Vanicek, T. J. Ansell, and S. F. B. Tett, 2006: Improved analyses of changes and uncertainties in sea surface temperature measured in situ since the mid-nineteenth century: The HadSST2 dataset. *J. Climate*, **19**, 446–469, <https://doi.org/10.1175/JCLI3637.1>.
- Robock, A., 2000: Volcanic eruptions and climate. *Rev. Geophys.*, **38**, 191–219, <https://doi.org/10.1029/1998RG000054>.
- , 2002: Pinatubo eruption: The climatic aftermath. *Science*, **295**, 1242–1244, <https://doi.org/10.1126/science.1069903>.
- , and J. Mao, 1992: Winter warming from large volcanic eruptions. *Geophys. Res. Lett.*, **19**, 2405–2408, <https://doi.org/10.1029/92GL02627>.
- Rotstayn, L. D., M. A. Collier, M. R. Dix, Y. Feng, H. B. Gordon, S. P. O’Farrell, I. N. Smith, and J. Syktus, 2009: Improved simulation of Australian climate and ENSO-related rainfall variability in a global climate model with an interactive aerosol treatment. *Int. J. Climatol.*, **30**, 1067–1088, <https://doi.org/10.1002/JOC.1952>.
- Santer, B. D., and Coauthors, 2014: Volcanic contribution to decadal changes in tropospheric temperature. *Nat. Geosci.*, **7**, 185–189, <https://doi.org/10.1038/ngeo2098>.
- Sato, M., J. E. Hansen, M. P. McCormick, and J. B. Pollack, 1993: Stratospheric aerosol optical depths, 1850–1990. *J. Geophys. Res.*, **98**, 22 987–22 994, <https://doi.org/10.1029/93JD02553>.
- Schmidt, G. A., and Coauthors, 2014: Configuration and assessment of the GISS ModelE2 contributions to the CMIP5 archive. *J. Adv. Model. Earth Syst.*, **6**, 141–184, <https://doi.org/10.1002/2013MS000265>.
- Sear, C. B., P. M. Kelly, P. D. Jones, and C. M. Goodess, 1987: Global surface-temperature responses to major volcanic eruptions. *Nature*, **330**, 365–367, <https://doi.org/10.1038/330365a0>.
- Self, S., M. R. Rampino, J. Zhao, and M. G. Katz, 1997: Volcanic aerosol perturbations and strong El Niño events: No general correlation. *Geophys. Res. Lett.*, **24**, 1247–1250, <https://doi.org/10.1029/97GL01127>.
- Soden, B. J., R. T. Wetherald, G. L. Stenchikov, and A. Robock, 2002: Global cooling after the eruption of Mount Pinatubo: A test of climate feedback by water vapor. *Science*, **296**, 727–730, <https://doi.org/10.1126/science.296.5568.727>.
- Stenchikov, G. L., I. Kirchner, A. Robock, H.-F. Graf, J. C. Antuña, R. G. Grainger, A. Lambert, and L. Thomason, 1998: Radiative forcing from the 1991 Mount Pinatubo volcanic eruption. *J. Geophys. Res.*, **103**, 13 837–13 857, <https://doi.org/10.1029/98JD006693>.
- , A. Robock, V. Ramaswamy, M. D. Schwarzkopf, K. Hamilton, and S. Ramachandran, 2002: Arctic Oscillation response to the 1991 Mount Pinatubo eruption: Effects of volcanic aerosols and ozone depletion. *J. Geophys. Res.*, **107**, 4803, <https://doi.org/10.1029/2002JD002090>.
- , K. Hamilton, R. J. Stouffer, A. Robock, V. Ramaswamy, B. Santer, and H.-F. Graf, 2006: Arctic Oscillation response to volcanic eruptions in the IPCC AR4 climate models. *J. Geophys. Res.*, **111**, D07107, <https://doi.org/10.1029/2005JD006286>.
- Stevenson, S., J. T. Fasullo, B. L. Otto-Bliesner, R. A. Tomas, and C. Gao, 2017: Role of eruption season in reconciling model and

- proxy responses to tropical volcanism. *Proc. Natl. Acad. Sci. USA*, **114**, 1822–1826, <https://doi.org/10.1073/pnas.1612505114>.
- Taylor, K. E., R. J. Stouffer, and G. A. Meehl, 2012: An overview of CMIP5 and the experiment design. *Bull. Amer. Meteor. Soc.*, **93**, 485–498, <https://doi.org/10.1175/BAMS-D-11-00094.1>.
- Thompson, D. W. J., and J. M. Wallace, 2001: Regional climate impacts of the Northern Hemisphere annular mode. *Science*, **293**, 85–89, <https://doi.org/10.1126/science.1058958>.
- , —, P. D. Jones, and J. J. Kennedy, 2009: Identifying signatures of natural climate variability in time series of global-mean surface temperature: Methodology and insights. *J. Climate*, **22**, 6120–6141, <https://doi.org/10.1175/2009JCLI3089.1>.
- Timmreck, C., 2012: Modeling the climatic effects of large explosive volcanic eruptions. *Wiley Interdiscip. Rev.: Climate Change*, **3**, 545–564, <https://doi.org/10.1002/WCC.192>.
- Trenberth, K. E., 2002: Evolution of El Niño–Southern Oscillation and global atmospheric surface temperatures. *J. Geophys. Res.*, **107**, 4065, <https://doi.org/10.1029/2000JD000298>.
- , and J. T. Fasullo, 2013: An apparent hiatus in global warming? *Earth's Future*, **1**, 19–32, <https://doi.org/10.1002/2013EF000165>.
- Voldoire, A., and Coauthors, 2013: The CNRM-CM5.1 global climate model: Description and basic evaluation. *Climate Dyn.*, **40**, 2091–2121, <https://doi.org/10.1007/s00382-011-1259-y>.
- Watanabe, M., and Coauthors, 2010: Improved climate simulation by MIROC5. Mean states, variability, and climate sensitivity. *J. Climate*, **23**, 6312–6335, <https://doi.org/10.1175/2010JCLI3679.1>.
- Watanabe, S., and Coauthors, 2011: MIROC-ESM 2010: Model description and basic results of CMIP5-20c3m experiments. *Geosci. Model Dev.*, **4**, 845–872, <https://doi.org/10.5194/gmd-4-845-2011>.
- Wu, T. W., and Coauthors, 2013: Global carbon budgets simulated by the Beijing Climate Center Climate System Model for the last century. *J. Geophys. Res. Atmos.*, **118**, 4326–4347, <https://doi.org/10.1002/JGRD.50320>.
- Yukimoto, S., 2011: Meteorological Research Institute Earth System Model version 1 (MRI-ESM1): Model description. Meteorological Research Institute Tech. Rep. 64, 88 pp.
- , and Coauthors, 2012: A new global climate model of the Meteorological Research Institute: MRI-CGCM3—Model description and basic performance. *J. Meteor. Soc. Japan*, **90A**, 23–64, <https://doi.org/10.2151/jmsj.2012-A02>.
- Zambri, B., and A. Robock, 2016: Winter warming and summer monsoon reduction after volcanic eruptions in Coupled Model Intercomparison Project 5 (CMIP5) simulations. *Geophys. Res. Lett.*, **43**, 10 920–10 928, <https://doi.org/10.1002/2016GL070460>.
- Zanchettin, D., and Coauthors, 2016: The Model Intercomparison Project on the climatic response to Volcanic forcing (VolMIP): Experimental design and forcing input data for CMIP6. *Geosci. Model Dev.*, **9**, 2701–2719, <https://doi.org/10.5194/gmd-9-2701-2016>.
- Zhao, M., I. M. Held, S.-J. Lin, and G. A. Vecchi, 2009: Simulations of global hurricane climatology, interannual variability, and response to global warming using a 50-km resolution GCM. *J. Climate*, **22**, 6653–6678, <https://doi.org/10.1175/2009JCLI3049.1>.